Environmental Science & Technology

Article

Cite This: Environ. Sci. Technol. 2019, 53, 3773−3781

pubs.acs.org/est

Integrating Biolayer Interferometry, Atomic Force Microscopy, and Density Functional Theory Calculation Studies on the Affinity between Humic Acid Fractions and Graphene Oxide

Qixing Zhou,*[,†] Shaohu Ouyang,[†] Zhimin Ao,[‡] Jing Sun,[†] Guanlan Liu,[‡] and Xiangang Hu[†]

[†]Key Laboratory of Pollution Processes and Environmental Criteria (Ministry of Education)/Tianjin Key Laboratory of Environmental Remediation and Pollution Control, College of Environmental Science and Engineering, Nankai University, Tianjin 300350, China

[‡]Guangzhou Key Laboratory of Environmental Catalysis and Pollution Control, Institute of Environmental Health and Pollution Control, School of Environmental Science and Engineering, Guangdong University of Technology, Guangzhou, 510006, China

Supporting Information

ABSTRACT: The interactions between nanoparticles and humic acid (HA) are critical to understanding the environmental risks and applications of nanoparticles. However, the interactions between HA fractions and graphene oxide (GO, a popular carbon nanosheet) at the molecular level remain largely unclear. Four HA fractions with molecular weights ranging from 4.6 to 23.8 kDa were separated, and the large HA fractions presented low oxygen contents and many aromatic structures. The binding constants of the large HA fractions on GO were 2.6- to 3551-fold higher than those of the small HA fractions, while the maximum adsorption capacities of the larger HA fractions onto GO were much higher. Atomic force microscopy (AFM) found that the small and large HA fractions were spread over the center and the edge of the GO nanosheets, respectively. Density functional theory (DFT) simulation and nuclear magnetic resonance spectroscopy confirmed the above phenomena (three adsorption patterns, "vs", "ps", and "pea") and revealed that HA bonded to the GO nanosheets mainly through van der Waals force and $\pi-\pi$ interactions. The integrating analysis of binding affinity, AFM, and DFT provides new insights into the environmental behavior of GO and the applications of GO in pollutant removal under exposure from HA.

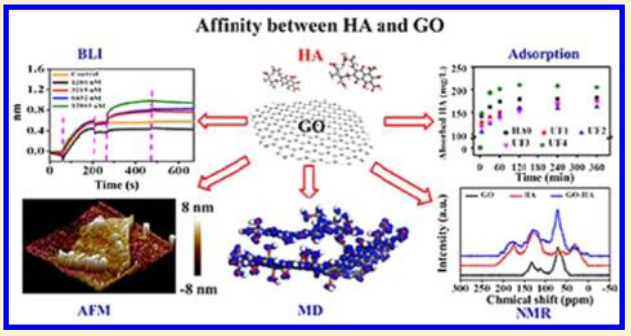

INTRODUCTION

Humic acid (HA), which has abundant functional groups (e.g., carboxylic, phenolic, alcoholic, and quinoid groups), is distributed widely in the natural environment.[1,2] HA plays a critical role in the environmental behavior of nanoparticles and determines the risks of nanoparticle applications via adsorption, photocatalysis, and passivation.[3−6] HA fractions present various sizes, chemical groups, and other properties, and exploring the interactions between nanoparticles and HA fractions (rather than mixed HA) is essential for understanding the environmental fate and effective applications of nanoparticles.[7,8] In recent years, the industrial application of graphene-family nanomaterials (GFNs) has developed rapidly; for example, the production of GFNs in China was estimated to be 400 tons, including 100 tons of graphene oxide (GO), in 2014.[9] GO is widely used in chemistry, physics, medicine, biology, manufacturing, and environmental protection due to its excellent properties.[10−14] However, the interactions between HA fractions and GO at the molecular level remain largely unclear.

Many reports have involved the adsorption of HA on GFNs: for example, Lee et al. studied the adsorption behaviors of humic-like components and revealed that larger-sized aromatic components within HA had a higher adsorption affinity compared to smaller-sized fractions.[15] However, the real-time affinity, the sites of affinity, and the interaction mechanisms of HA fractions with GO remain largely unknown.[16,17] Biolayer interferometry (BLI) is a real-time and label-free optical technique that uses fiber-optic biosensors to measure the interactions between biomolecules, such as protein−protein, protein−nucleic acids, and protein−small molecules.[18,19] In recent years, BLI has been rapidly developed and used to successfully investigate GO−proteins and GO−single-stranded DNA (ssDNA) interactions.[20−22] Here, BLI will be used to explore the binding affinity between GO and HA. Furthermore, identifying the favorable adsorption sites of HA is critical to the design of adsorbent materials, because HA adsorption affects the environmental behaviors and functions of adsorbents.[23,24] Atomic force microscopy (AFM) can directly

Received: September 17, 2018
Revised: January 22, 2019
Accepted: March 13, 2019
Published: March 13, 2019

DOI: 10.1021/acs.est.8b05232
Environ. Sci. Technol. 2019, 53, 3773−3781

observe the binding sites of HA fractions on GO.[25] However, the specific interactions between GO and HA at the molecular level need further investigation. Herein, density functional theory (DFT) simulations integrated with AFM, nuclear magnetic resonance (NMR) spectroscopy, and Fourier transform infrared (FTIR) spectroscopy were employed to explore the intensity and sites of affinity of HA on GO.

Prior to examining the specific interactions between GO and HA fractions, the different HA fractions should be sized. Many techniques, such as gel chromatography, ultrafiltration, density gradient centrifugation, and size-exclusion chromatography, have been used to fractionate HA samples in terms of their solubility, molecular weight (Mw) or size, charge density, and adsorption properties.[5,26−28] Tangential flow ultrafiltration (TFU) is a powerful ultrafiltration method to select for size and concentrate target species because of its potential reduction of infiltration artifacts and efficacy for size selection.[29,30] Herein TFU is used to isolate HA fractions. To systematically characterize the chemical and molecular heterogeneity of fractionated HA, high-performance size-exclusion chromatography (HPSEC) combined with UV−vis spectroscopy, fluorescence excitation−emission matrices (EEMs), and electron paramagnetic resonance (EPR) is performed in the present work. In summary, integrating BLI, AFM, NMR, and DFT to study the affinity between HA fractions and GO provides deep insight into the environmental behaviors of GO and the removal of HA contamination by GO-enabled membranes or catalysis.

MATERIALS AND METHODS

Fractionation of HA by TFU. HA (product number H811077) was obtained from Shanghai Macklin Biochemical Co., Ltd. HA was dissolved in Milli-Q water (1000 mg/L), and the resulting solution was adjusted to pH 10.0 with 0.1 M NaOH. Then the HA solution was sonicated at 100 W, 40 kHz, and 25 °C for 30 min. After magnetic stirring for 24 h, the HA solution was filtered through a 0.22 μm membrane filter. The final total organic C (TOC) concentration of the original HA (HA0) was 370 ± 20 mg_C/L, as measured by a TOC analyzer (multi N/C3100, Analytikjena, Germany). The TFU technique (Sartorius, German) was used to fractionate HA0 into four fractions. The ultrafiltration process combined diafiltration and concentration.[31,32] The TFU (Vivaspin Turbo 15, Sartorius, German) cut off at molecular weights of 3, 10, and 30 kDa. A schematic of the HA fractionation procedure is illustrated in Figure S1. TFU separation was achieved in three parallel samples. Finally, the four HA fractions, UF1 (<3 kDa), UF2 (3−10 kDa), UF3 (10−30 kDa), and UF4 (>30 kDa) were obtained and then acidified to pH ∼ 7 with 0.1 M HCl.

Characterization of the GO and HA Fractions. Graphene oxide (GO, product number XF002-1) with a purity >99 wt %, lateral dimensions of 0.5−5 μm, and height of 0.8−0.9 nm was purchased from Nanjing XFNANO Materials Tech Co., Ltd. (China). GO (50.0 mg) and 500 mL Milli-Q water in a 1000 mL flask (total of six flasks) were sonicated for 30 min at 100 W and 35 kHz in ice−water. Details of the characterization of GO and the HA fractions are provided in Supporting Information (SI).

Binding Affinity Measurements. BLI was used to quantitatively characterize the binding interactions between the GO sheets and HA fractions. Here the BLI measurements were performed on a ForteBio OctetRED96 System (Pall ForteBio Corp., Fremont, CA). GO easily bound to the aminopropylsilane (APS) tips (ForteBio, USA) because of noncovalent loading and hydrophobic interactions.[21] An adequate amount of the GO suspension (200 μL, 100 mg/L) was loaded onto the APS tips, and then the GO-loaded tips were washed with PBS for balance and transferred to wells containing different concentrations of fractionated HA. PBS was used as a reference and dilution buffer. The total working volume of the samples and buffer was 200 μL in 96-well plates (product number C0221A, Greiner bio-one, Germany) with a shake speed of 1000 rpm. All binding data were collected at 25 °C. The APS biosensor tips were prewetted for 10 min in PBS buffer prior to assay. The working procedure contained five steps: baseline acquisition for 60 s, GO loading onto the APS sensor for 150 s, a second baseline acquisition for 60 s, association measurement of the association rate (k_{on}) for 200 s, and dissociation measurement of the dissociation rate (k_{off}) for 200 s. Given the detection range (1−40 mg_C/L) of the instrument, different concentrations (2.0, 5.0, 10.0, 15.0, 20.0, and 30.0 mg_C/L) of the HA0 and HA fractions were chosen. The baseline and dissociation steps were carried out in buffer only. Finally, the kinetic parameters (k_{on} and k_{off}) were calculated using Data Analysis Software 8.0. The binding constant (K_D) was calculated from the ratio of k_{on} to k_{off}.

Aggregation Kinetics of GO. The variation in the hydrodynamic diameter (D_h) of GO and the GO−HA fractions were measured using a ZETAPALS/BI-200SM instrument equipped with a 30 mW, 635 nm laser (Brookhaven Instruments Corporation, Holtsville, NY). The details are presented in SI.

Adsorption Experiments. In the adsorption experiments, the concentration of GO was 10 mg/L, and the concentration of the HA solutions ranged from 0 to 20 mg_C/L. The final volume was 10 mL. The pH of each sample was adjusted to 7.0 using 0.01 M NaOH or 0.01 M HCl. Incubation was performed at 60 r/min for 24 h on a rotator (MX-RL-Pro, Dragon Laboratory Instruments Limited, China) at 25 ± 1 °C prior to centrifugation at 14 000g for 10 min. The contents of free HA in the supernatant were passed through a 0.22 μm membrane filter and then measured via UV−vis spectroscopy at 254 nm (Abs_{254}). A calibration curve between the HA concentrations and Abs_{254} was obtained using a wide range (1.25 to 20.0 mg_C/L) of HA concentrations. The details of the adsorption experiments are provided in SI. Pseudo-first-order and pseudo-second-order kinetics models were used to analyze the adsorption kinetics of GO. The sorption isotherms were fitted by the Langmuir and Freundlich models. The details of the adsorption kinetics and isotherm experiments are presented in SI.

FTIR, Solid-State ^{13}C NMR, EPR, and AFM Analysis. The tested concentration of both GO and HA was 10 mg/L. GO sheet suspensions were mixed with an equal volume of fractionated HA solution and constantly shaken at 60 r/min for 24 h at room temperature. After centrifugation at 14 000g for 10 min, the GO−HA conjugates were washed with Milli-Q water to remove the unbound HA fraction until there was no color in the washing water and dried at room temperature. GO after adsorption with fractionated HA was freeze-dried before FTIR characterization, and 0.1 mg of the GO−HA conjugates was lyophilized prior to mixing with KBr powder (100 mg). The FTIR spectra were recorded on a Bruker Tensor 27 infrared spectrometer (Germany) in the 4000−400 cm^{-1} region with a resolution of 4 cm^{-1} in transmission mode.

DOI: 10.1021/acs.est.8b05232
Environ. Sci. Technol. 2019, 53, 3773−3781

Solid-state ^{13}C NMR was employed to characterize the interactions between HA and GO and GO−HA. Solid-state ^{13}C cross-polarization magic-angle spinning (CPMAS) NMR spectra were recorded on an Agilent 600 DD2 instrument (Agilent, Santa Clara, CA) equipped with a 4 mm MAS probe at a resonance frequency of 150.15 MHz. The ^{13}C CPMAS NMR spectra of GO, HA, and GO−HA were collected with a spinning rate of 15 kHz, a delay time of 5 s, and a scan number of 2048. The unpaired electrons of HA, GO, and GO−HA were examined on a Magnettech MiniScope 400 spectrometer (Germany) (details are provided in SI). AFM was used to observe the morphology of GO before and after the adsorption of HA0 and different HA fractions. AFM images of the GO−HA conjugates were obtained using a Dimension Icom AFM instrument (Bruker, Billerica, MA) in tapping mode.

Density Functional Theory Simulations. Density functional theory (DFT) calculations were performed using the DMol3 code.[33] Because the local density approximation (LDA) overestimates the bond energy and underestimates equilibrium distances,[34] the generalized-gradient approximation (GGA) and the Perdew−Burke−Ernzerhof (PBE) method were adopted to treat the correlation.[35] The DFT semicore pseudopotentials (DSPP) core treatment was used treat relativistic effects.[36] The k-point mesh was set to 3 × 3 × 1. The convergence criterion for the energy and electron density was 1.0×10^{-5} a.u., and that for the maximum force was 0.002 Ha/Å. Self-consistent field (SCF) tolerance was carried out with a convergence criterion of 1.0×10^{-6} a.u. The same conditions were adopted in all the calculations to ensure that the results were comparable. The modified HA model proposed by Sein et al. was used,[37] which contains typical hydrophobic character, mainly as aromatic rings, OH, and COOH of HA. Due to the limitations of the DFT calculation method and computing speed, DFT calculation is generally suitable for systems containing a few hundred or, at most, a few thousand atoms.[33,38] Thus, the molecules must be simplified in actual simulations. The GO model used referred to a previous study[39,40] and contained 128 atoms. The functional groups, such as OH, COOH, and semiquinone, were distributed randomly on both sides of the GO layer. To model the interaction sites between HA and GO, HA was placed vertically or parallel on the surface or zigzag on the edge of GO. Then the total energy of the whole system was compared to determine the most stable structure. The adsorption energy E_a between HA and GO was defined as

$$E_a = E_{total} - (E_{GO} + E_{HA}) \quad (1)$$

where E_a, E_{total}, E_{GO}, and E_{HA} are the adsorption energy and the energies of GO with the adsorbed HA, GO, and HA, respectively. The population analysis was calculated to analyze the charge transfer between GO and HA. The electron density was also calculated to understand the interaction between GO and HA.

Statistical Analysis. All experiments were performed in triplicate, and the results are presented as the mean ± standard deviation. One-way analysis of variance (ANOVA) with Tukey's test was employed to analyze the significant differences. Pseudo-first-order and pseudo-second-order kinetics models and the Langmuir and Freundlich models were determined using Origin 8.0 software. The AFM images were analyzed with NanoScope Analysis 1.8 software. The density functional theory simulation was conducted by DMol3 code.

RESULTS AND DISCUSSION

Characterization of GO and Fractionated HA. The XPS spectrum showed that GO contained C−C (49%), C−O (35%), C═O (12%), and O═C−C (4%) bonds, as we previously reported.[41] The distributions of carbon and oxygen on GO are shown by TEM elemental mapping in Figure S2a−d. The AFM images of GO are shown in Figure S2e,f. GO presented a nanosheet morphology with an average thickness of 1.05 ± 0.20 nm (n = 6).

Separated by TFU and HPSEC chromatograms, the HA0 and HA fractions showed apparent increases in Mw ranging from 4.6 to 23.8 kDa (Figure S3 and Table S1). The characteristics (e.g., molecular weight and percentages of C, O, and H) of the HA fractions separated by TFU and HA0 are listed in Table S1. UF1, UF2, UF3 and UF4 accounted for 65.6%, 7.6%, 4.8%, and 22.0% of the total mass of HA0, respectively. The carbon contents were lower in HA0 and the small fractions UF1−UF3 than in the large fraction UF4. The results of UV−vis absorbance (such as the E_2/E_3 ratio and SUVA $_{254}$) and excitation−emission matrices (EEMs) fluorescence analysis of the HA0 and HA fractions are provided in Table S1 and Figure S4, respectively (a detailed description is also presented in SI).

The FTIR spectra of the HA0 and HA fractions are shown in Figure S5, indicating that the structures and functional groups of the four HA fractions were similar to those in a typical HA FTIR spectrum.[4] Furthermore, the I_{1630}/I_{2920} ratio ("carboxylates" to aliphatics) and carbonyl index (CI) were used to reflect the degree of humification and the population of carbonyl groups (C═O) in HA, respectively.[31,42,43] As shown in Table S2, the I_{1630}/I_{2920} ratio of the large fraction UF4 (2.6) was significantly ($p < 0.05$) larger than that of HA0 (1.2) and the small fractions UF1−UF3 (1.3−1.6), and the increase in the I_{1630}/I_{2920} ratio could be explained by the increase in aromaticity.[44] On the other hand, the CI values of the large fraction UF4 (1.4) was significantly ($p < 0.05$) lower than that of the small fractions UF1−UF3 (2.0−2.9), suggesting that the large fraction UF4 had fewer carbonyl functional groups than the small fractions UF1−UF3 (Table S2). In Figure S6, the g-values for the HA0 and HA fractions ranged from 2.0052 to 2.0064, representing an EPR semiquinone-type free radical signal in the HA samples.[45] The concentration of stable semiquinone-type free radicals in the large fraction UF4 was higher than that in the small fractions UF1−UF3. A possible explanation is the low content of aromatic rings in the small fractions UF1−UF3 compared to the large fraction UF4.

Effects of HA Molecular Weight on Binding Affinity to GO. The strong interactions (noncovalent loading and hydrophobic interactions) of APS with GO formed a stable GO layer on the surface of the APS sensor tip.[21] The GO-coated APS sensors were then incubated with four HA fractions over a concentration gradient to measure the corresponding association and dissociation signals (Figure S7a). The step parameters and assay times of BLI measurement are listed in Figure S7b. The BLI binding affinity for all HA fractions to GO were collected, and the differences between signal intensities were observed. For the control containing GO alone, no significant signal differences were observed, while the association and dissociation kinetics of UF1 to GO were obviously observed, indicating effective binding, as evident from the GO−APS sensor (Figure S7c). The association−dissociation curves of the binding of HA0

DOI: 10.1021/acs.est.8b05232
Environ. Sci. Technol. 2019, 53, 3773−3781

and the four HA fractions onto GO are shown in Figure 1a–e. The corresponding association and dissociation parameters are

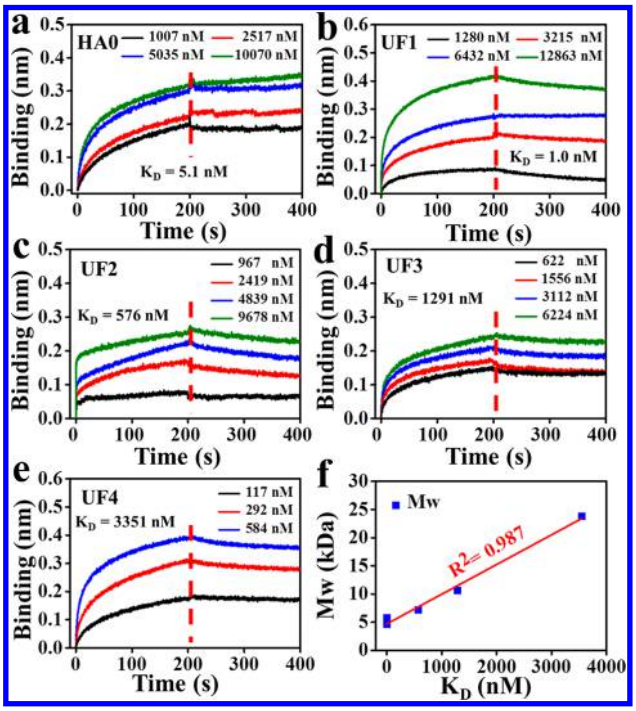

Figure 1. Biolayer interferometry affinity measurements. (a–e) Association and dissociation curves of HA0 (the original HA without fractionation) and HA fractions on GO nanosheets. (f) Linear correlation between the binding constant (K_D) and the molecular weight of HA0 and the HA fractions.

listed in Table S3. As the Mw of the HA fractions increased, the association or adsorption rate (k_{on}) of HA onto the GO surface increased (Table S3), suggesting that higher-Mw HA had a higher adsorption binding affinity to GO, which is consistent with previous reports.[15,46,47] The above observation might be attributed to the structural differences between the HA fractions, especially to the higher contents of aromatic structure components in the larger fractions of HA (Table S1 and Figure S6). The benzene rings in the aromatic structure of HA increased the adsorption affinity of HA to GO or CNTs.[46,48,49] Similarly, the disassociation rate (K_{off}) of HA from GO increased with the Mw of HA (Table S3). Furthermore, the binding constant (K_D) increased with the apparent Mw of HA0 and the HA fractions: K_D (UF1) < K_D (HA0) < K_D (UF2) < K_D (UF3) < K_D (UF4). The K_D values had a negative correlation with the affinities.[50] Thus, UF3 (K_D = 576 nM) and UF2 (K_D = 1291 nM) bound approximately 3-fold and 6-fold more tightly than did UF4 (K_D = 3351 nM), respectively, and UF1 (K_D = 1 nM) bound approximately 3351-fold more tightly than UF4 (Figure 1b–e). The affinity of HA to GO was obviously greater than those of immunoglobulin (K_D = 767 nM), transferrin (K_D = 3660 nM), and bovine serum albumin (K_D = 6410 nM) to GO.[20] The BLI experiment revealed that the Mw of HA played an important role in the binding affinity of HA to GO, and Figure 1f confirms that there was a positive linear relationship between the HA Mw and K_D (R^2 = 0.987).

GO Aggregation Affected by HA Fractions. The initial D_h of GO was approximately 520 nm, which increased rapidly to ~1100 nm at 2000 s (Figure S8). In contrast, the inclusion of HA0 and the HA fractions kept the D_h of GO at 600–1000 nm, which is consistent with previous reports by Chowdhury et al.[51] As expected, the nanoparticle D_h and aggregation of the small HA fractions (UF1-UF3) were reduced over those of the large HA fraction (UF4). The aggregation rate constants ($K\alpha$) of pristine GO and GO–UF4 in Milli-Q water were 0.361 and 0.114 nm/s, respectively (Figure S8), indicating that the stability of GO improved significantly in the presence of HA (10 mg_C/L). The above result was consistent with our previous study.[52,53] Furthermore, Figure S9 shows that the $K\alpha$ of GO aggregation was negatively correlated with the Mw of HA (R^2 = 0.900), suggesting that the high content of aromatic rings in the large fraction UF4 (Table S1 and Figure S5) probably led to the high stability of GO via steric repulsion.

Adsorption Kinetics and Isotherms of HA on GO. The amount of HA absorbed on GO was determined by the UV–vis absorbance at 254 nm (Abs_{254}) (details are provided in SI), and the calibration curve between Abs_{254} and the concentration of HA0 and the HA fraction is presented in Figure S10. Because GO (0.5–5 μm) was removed after centrifugation at 14 000g for 10 min and filtered through a 0.22 μm membrane, GO did not affect the determination of HA at Abs_{254}. The adsorption kinetics of HA0 and the four HA fractions absorbed onto GO are shown in Figure 2a. The adsorption capacity of

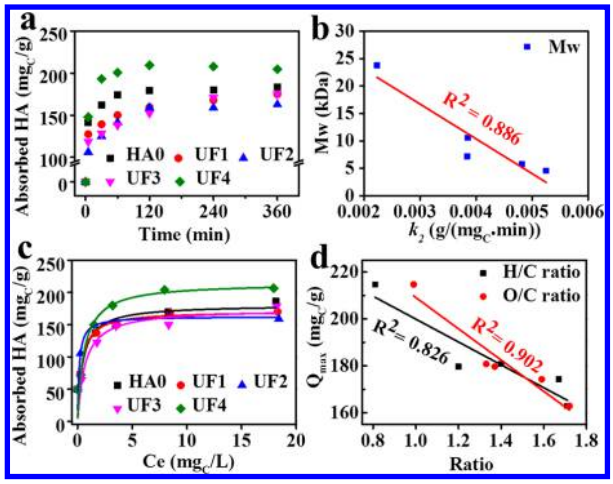

Figure 2. Quantitative analysis of the adsorption of HA0 and the HA fractions on GO. (a) Adsorption kinetics of HA0 and the HA fractions onto GO. (b) Linear correlation between the pseudo-second-order constant (k_2) and the molecular weight of HA. (c) Adsorption isotherms of HA0 and the HA fractions adsorbed onto GO, with the solid lines representing isotherms fitted using the Langmuir model. (d) Linearity correlations between the elemental ratio of HA0 and the HA fractions and the maximum adsorption capacities (Q_{max}) of HA on GO.

the HA fractions on GO increased rapidly in the first 1 h and reached adsorption equilibrium at approximately 4 h. The pseudo-second-order model fit the adsorption kinetics of the HA fractions onto GO better than the pseudo-first-order model, as presented in Table S4, suggesting that in addition to flat surface adsorption, the adsorption on GO was rate-limiting. The fast kinetics are in accordance with previous adsorption studies (e.g., polycyclic aromatic hydrocarbons) with GO.[54] The k_2 of the pseudo-second-order model decreased from 0.00525 to 0.00254 g/(mg_C·min) as the HA fraction size increased. Nanosize effects of HA samples may play an important role in the adsorption kinetics because the

DOI: 10.1021/acs.est.8b05232
Environ. Sci. Technol. 2019, 53, 3773–3781

accessibility of adsorption sites on GO for HA molecules is dependent on the molecular size.[55] Further quantitative analysis between the Mw of HA and k_2 is plotted in Figure 2b. The k_2 values of the HA fractions were negatively correlated with the Mw (R^2 = 0.886), and the k_2 values of HA0 and the small fractions UF1-UF3 were larger than that of the large fraction UF4 (Figure 2b), indicating that small-sized HA quickly adsorbed onto the GO surface. In addition, the binding affinity of GO for HA molecules was dependent on the Mw of HA (Figure 1), which may also play an important role in the adsorption kinetics.

The adsorption isotherms of the four HA fractions onto GO are shown in Figure 2c. The Langmuir and Freundlich models were used to fit the isotherms, and the corresponding regression parameters are listed in Table S5. According to the regression coefficient (R^2), the isotherms of the HA fractions are well fitted by the Langmuir and Freundlich models, which means that the isotherms of the HA fractions on GO are nonlinear and the adsorption sites are homogeneously distributed over the GO surface. The above results were confirmed by the following AFM and DFT analyses. Moreover, the maximum adsorption capacity (Q_{max}) of the large fraction UF4 onto GO was 214.7 mg_C/g, which was much higher than that of the small fractions UF1 (171.0 mg_C/g), UF2 (162.9 mg_C/g) and UF3 (174.3 mg_C/g). To reveal the interaction mechanisms, the correlations between the Q_{max} values of HA on GO and the H/C and O/C ratios of HA were also plotted and are given in Figure 2d. The Q_{max} values were negatively correlated with the H/C and O/C ratios of the HA fractions (R^2 = 0.826 and 0.902, respectively). An increase in the H/C and O/C ratios indicated a decrease in the number of aromatic structures in the HA fraction (Table S1). Thus, the aromatic structures of HA likely contributed to the high adsorption capacity of the large HA fractions on GO, indicating that the $\pi-\pi$ interactions between the GO and HA molecules might play an important role in adsorption.

To analyze the interactions between HA0, the HA fractions, and GO, the FTIR spectra of GO before and after the adsorption of HA were measured and are shown in Figure 3a. Compared with the GO spectrum before HA adsorption, the peaks of the H-bonded OH stretch shifted from 3420 to 3450 cm^{-1}, and the intensity increased significantly after the adsorption of HA fractions onto GO, which indicates that H-bonding plays an important role in the adsorption process between GO and HA. In addition, the positions of the C═O and O−H or C−O (carboxylic group) stretching vibrations of GO clearly changed after interaction with HA. The peaks corresponding to C═C bonds shifted from 1623 to 1635 cm^{-1}, implying that $\pi-\pi$ interactions contributed to the adsorption of HA on GO. To further confirm the $\pi-\pi$ interactions of GO−HA, solid-state ^{13}C NMR was performed. NMR has been widely used in HA and GO structural studies.[56,57] As shown in Figure 3b, compared with GO, aliphatic C (0−50 ppm), phenolic C (145−162 ppm), and C═O/COOH (162−220 ppm) peaks were observed in the both HA and GO−HA sample, indicating that HA was immobilized on GO. Moreover, the aromatic group peak of GO at 132 ppm shifted to 128 ppm for GO−HA, suggesting that the aromatic groups of HA coupled with the GO sp^2 structure through $\pi-\pi$ interactions, which was consistent with the FTIR results shown in Figure 3a. Furthermore, the EPR spectra of GO, HA, and GO−HA were obtained under the same conditions, as shown in Figure S11. The *g*-values of GO,

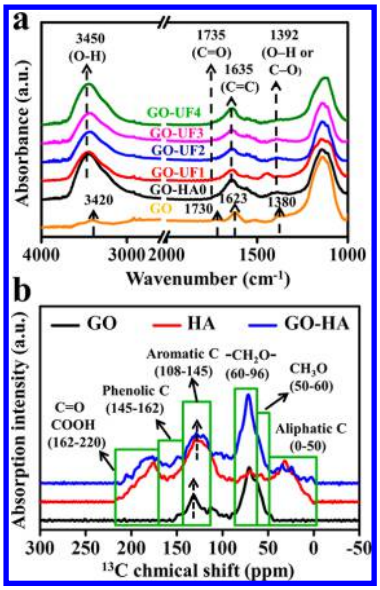

Figure 3. FTIR spectra of GO before and after the adsorption of HA0 and the HA fractions (a) and solid-state ^{13}C NMR spectra of HA, GO, and GO−HA (b).

HA, and GO−HA were 2.0062, 2.0058, and 2.0055, respectively. HA and GO−HA had a greater width of the resonance line and a higher signal intensity than the GO-alone control, suggesting that GO−HA and HA had higher levels of semiquinone-type unpaired electrons than did GO (GO−HA > HA > GO). The level of semiquinone-type unpaired electrons measured by the EPR content were consistent with the content of aromatic groups obtained by NMR (Figure 3b).Therefore, the interactions between GO and the HA fractions, including $\pi-\pi$ and other interactions, were analyzed by the following DFT simulations.

Density Functional Theory Simulations. AFM is a useful tool for studying the distribution and morphology of HA adsorption on GO. Compared with pristine GO (Figure S2d), the observed thicknesses of GO coated by HA0 and the HA fractions increased from 4.2 to 10.4 nm (Figure S12) and from 4.5 to 24.3 nm (Figure S13), respectively. The largest thickness of GO coated by UF4 was consistent with the highest adsorption capacity of UF_4, as shown in Figure 2c and Table S5. Based on the AFM images in Figures 4a−d and S12, three adsorption patterns were observed between HA and GO: (i) most of the UF1 and small-sized UF2 (sizes from 5.6 to 11.2 nm, observed by AFM) were spread over the center and close to the edge of the GO nanosheets (denoted by the yellow circles in Figure 4a and 4b), (ii) most of the large-sized UF2 and small-sized UF3 (sizes from 5.6 to 11.2 nm) were spread over the center of the GO nanosheets (denoted by the red circles in Figure 4b and 4c), and (iii) most of the UF4 (sizes from 11.3 to 24.3 nm) was spread along the edge of the GO nanosheets (denoted by the blue circles in Figure 4d).

The above three phenomena were confirmed using DFT simulations (Figure 4e). The model structures of HA and GO are presented in Figures S14 and S15, respectively. In general, the effects of edge atoms on the inner atoms are negligible after 3 atomic layers.[58] For adsorption model I and adsorption model III, the HA was located on 2 to 8 atomic layers and 1 to 2 atomic layers near the edge of GO, respectively, and a bond order loss occurred. For adsorption model II, the HA was located on >3 atomic layers, and neither bond order loss nor

DOI: 10.1021/acs.est.8b05232
Environ. Sci. Technol. 2019, 53, 3773−3781

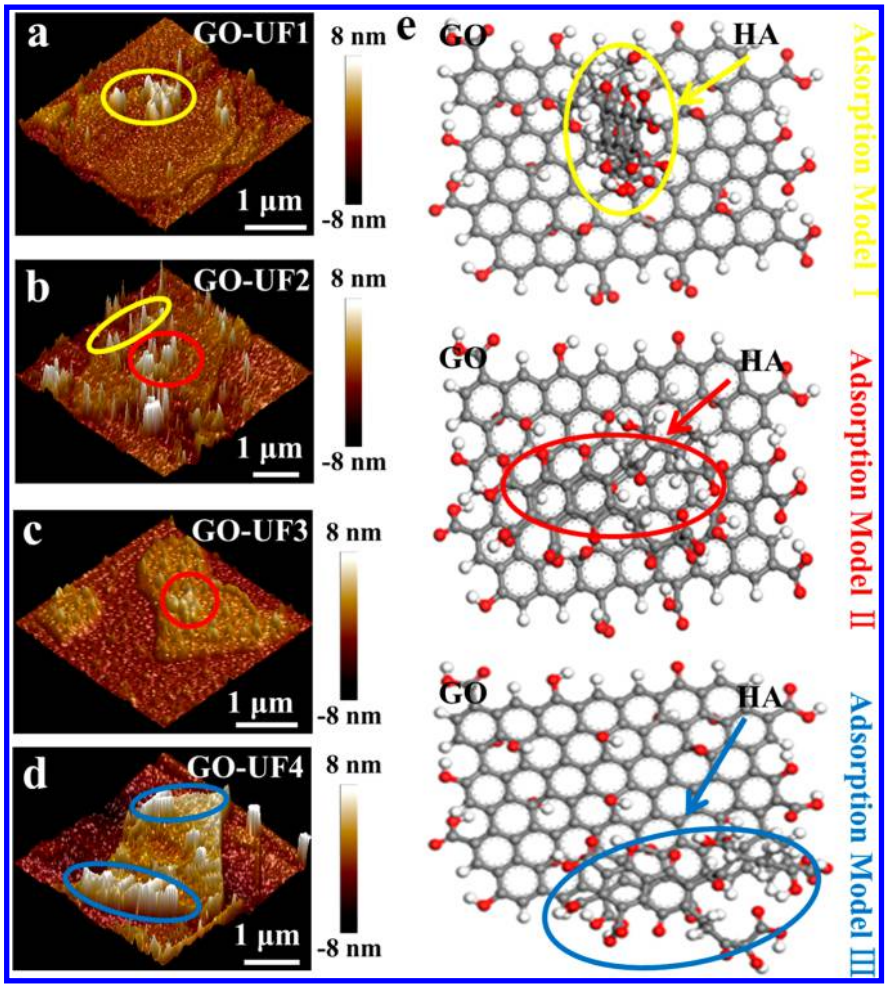

Figure 4. Interactions between HA fractions and GO illustrated by AFM and DFT simulations. (a–d) AFM images of HA fractions incubated with GO for 24 h. (e) DFT simulations of HA interacting with GO. Adsorption model I, HA spread over the center and close to edge of the GO nanosheet; adsorption model II, HA spread over the center of the GO nanosheet; adsorption model III, HA spread over the edge of the GO nanosheet, denoted by yellow, red, and blue arrows, respectively. HA was vertical to the surface of the GO nanosheet (vs), parallel to the surface of the GO nanosheet (ps) and parallel to the zigzag edge of the GO nanosheet (pez), which are consistent with adsorption models I, II, and III, respectively.

edge effects occurred. Furthermore, in adsorption model I, HA was vertical to the surface of the GO nanosheet (vs), and the interactive functional groups were mainly O-containing functional groups (OH and COOH), which interacted though $\pi-\pi$ interactions.[59] In contrast, in adsorption model II, HA was parallel to the surface of the GO nanosheet (ps), and the van der Waals force contributed to the binding of HA to GO and appeared to be the governing force.[60] In adsorption model III, HA was mostly parallel to the zigzag edge of the GO nanosheet (pez), and $\pi-\pi$ interactions contributed only a minor portion compared to the van der Waals force. To better understand the forces governing the spontaneous migration of HA to GO, the convergence tolerance of the energy E_b (eV) and the adsorption energy E_a (Ha) between HA and GO were calculated, as listed in Table S6. The adsorption energy E_b was −1.1564 eV, −2.7231 eV, and −2.2651 eV for structures "vs", "ps", and "pez", respectively (Table S6). Thus, the minimum diffusion barrier with the lowest adsorption energy was achieved for the structure "ps", indicating that "ps" was the most stable structure for HA adsorption on GO. The adsorption energy E_a was −0.0425 Ha, −0.1001 Ha, and −0.0832 Ha for structures "vs", "ps", and "pez", respectively, suggesting that HA in the "vs", "ps", and "pea" structure accepted 0.0425 e, 0.1001 e, and 0.0832 e from GO, respectively (Table S6). Therefore, the "ps" structure accepted more electrons from GO than the "vs" and "pea" structures, explaining the stable interaction of HA in the "ps" structure with GO. To gain further insight into the adsorption models and sites of HA on GO, the atomic charge density distribution was studied and is provided in Figure S16. No electronic cloud overlap was observed between HA and GO, which showed that the adsorption of HA on GO was weak with limited charge transfer, because of weak van der Waals force interactions between GO and HA. This result is consistent with adsorption pattern II observed in AFM.

Implications for Nanomaterial Risks and Applications. The extensive use of GO will inevitably lead to its release into the aqueous environment. Thus, knowledge of the interactions between GO and HA in water is urgently required to evaluate the environmental risks of GO. Herein, multiple analytical methods such as BLI, AFM, and DFT were integrated to investigate the adsorption affinity and favorable adsorption sites for HA fractions on GO. It was revealed that the Mw of HA was correlated to its binding affinity and adsorption rate onto GO, and the aromatic structure of HA determined its adsorption capacity and sites on GO. These

DOI: 10.1021/acs.est.8b05232
Environ. Sci. Technol. 2019, 53, 3773−3781

results are valuable for elucidating the environmental behaviors and functions of GO and other graphene-based materials under exposure from natural organic matter (NOM) with different properties. Moreover, the favorable adsorption sites and interaction mechanisms between HA and GO should be understood for GO enabled adsorbents, membranes, or catalysts in the contaminated water. DFT simulations and AFM imaging revealed that HA bonded to GO nanosheets mainly by van der Waals force and $\pi-\pi$ interactions. The proposed edge- and center-adsorption patterns support the effective design of GO-based surfaces. In addition, van der Waals force and $\pi-\pi$ interactions as two critical forces deserve attention for the removal of HA by GO-enabled membranes.

■ ASSOCIATED CONTENT

Supporting Information

The Supporting Information is available free of charge on the ACS Publications website at DOI: 10.1021/acs.est.8b05232.

Fractionation of HA by TFU (Figure S1). Characterization of GO (Figure S2) and fractionated HA (Figures S3−S6 and Tables S1 and S2). BLI experiments (Figure S7 and Table S3). Aggregation kinetics of GO (Figures S8 and S9). Adsorption experiments (Figure S10 and Tables S4 and S5). EPR spectra of HA, GO, and GO−HA (Figure S11). AFM images of HA0 and the HA fractions on GO (Figures S12 and S13). Adsorption models and density functional theory simulations of HA adsorption by GO (Figures S14−S16 and Table S6) (DOCX)

■ AUTHOR INFORMATION

Corresponding Author

*E-mail: zhouqx@nankai.edu.cn. Phone: +86-022-23507800. Fax: +86-022-66229562.

ORCID

Qixing Zhou: 0000-0003-2804-2360
Zhimin Ao: 0000-0003-0333-3727
Xiangang Hu: 0000-0002-9403-816X

Notes

The authors declare no competing financial interest.

■ ACKNOWLEDGMENTS

This work was financially supported by the National Natural Science Foundation of China (grant nos. 21677080, 21722703, 31770550, 21607029, and 21777033), the Ministry of Education (People's Republic of China) as an innovative team rolling project (grant no. IRT_17R58), a 111 program (grant no. T2017002), the Special Funds for Basic Scientific Research Services of Central Colleges and Universities, Science and Technology Program of Guangdong Province (2017B020216003), the Science and Technology Program of Guangzhou City (201707010359), the "1000 plan" for young professionals program of China, and the "100 talents" program of Guangdong University of Technology, the National Supercomputing Centre in Guangzhou (NSCC-GZ). The authors acknowledge the BLI data collection by Dr. Zengzhi Yuan of the Tianjin Key Laboratory of Animal and Plant Resistance, College of Life Sciences, Tianjin Normal University.

■ REFERENCES

(1) Long, M.; Brame, J.; Qin, F.; Bao, J.; Li, Q.; Alvarez, P. J. Phosphate changes effect of humic acids on TiO_2 photocatalysis: from inhibition to mitigation of electron-hole recombination. *Environ. Sci. Technol.* **2017**, *51* (1), 514−521.

(2) Jayalath, S.; Wu, H.; Larsen, S. C.; Grassian, V. H. Surface adsorption of suwannee river humic acid on TiO_2 nanoparticles: A study of pH and particle size. *Langmuir* **2018**, *34* (9), 3136−3145.

(3) Alimi, O. S.; Farner Budarz, J.; Hernandez, L. M.; Tufenkji, N. Microplastics and nanoplastics in aquatic environments: aggregation, deposition, and enhanced contaminant transport. *Environ. Sci. Technol.* **2018**, *52* (4), 1704−1724.

(4) Rashid, M.; Price, N. T.; Gracia Pinilla, M. A.; O'Shea, K. E. Effective removal of phosphate from aqueous solution using humic acid coated magnetite nanoparticles. *Water Res.* **2017**, *123*, 353−360.

(5) Milne, C. J.; Lapworth, D. J.; Gooddy, D. C.; Elgy, C. N.; Valsami-Jones, E. Role of humic acid in the stability of Ag nanoparticles in suboxic conditions. *Environ. Sci. Technol.* **2017**, *51* (11), 6063−6070.

(6) Chu, K. H.; Huang, Y.; Yu, M.; Her, N.; Flora, J. R. V.; Park, C. M.; Kim, S.; Cho, J.; Yoon, Y. Evaluation of humic acid and tannic acid fouling in graphene oxide-coated ultrafiltration membranes. *ACS Appl. Mater. Interfaces* **2016**, *8* (34), 22270−22279.

(7) Grillo, R.; Rosa, A. H.; Fraceto, L. F. Engineered nanoparticles and organic matter: A review of the state-of-the-art. *Chemosphere* **2015**, *119*, 608−619.

(8) Bian, S. W.; Mudunkotuwa, I. A.; Rupasinghe, T.; Grassian, V. H. Aggregation and dissolution of 4 nm ZnO nanoparticles in aqueous environments: Influence of pH, ionic strength, size, and adsorption of humic acid. *Langmuir* **2011**, *27* (10), 6059−6068.

(9) Zhu, Y.; Ji, H.; Cheng, H.-M.; Ruoff, R. S. Mass production and industrial applications of graphene materials. *Natl. Sci. Rev.* **2018**, *5* (1), 90−101.

(10) Amani, H.; Habibey, R.; Hajmiresmail, S. J.; Latifi, S.; Pazoki-Toroudi, H.; Akhavan, O. Antioxidant nanomaterials in advanced diagnoses and treatments of ischemia reperfusion injuries. *J. Mater. Chem. B* **2017**, *5* (48), 9452−9476.

(11) Mu, Q.; Su, G.; Li, L.; Gilbertson, B. O.; Yu, L. H.; Zhang, Q.; Sun, Y.-P.; Yan, B. Size-dependent cell uptake of protein-coated graphene oxide nanosheets. *ACS Appl. Mater. Interfaces* **2012**, *4* (4), 2259−2266.

(12) Akhavan, O.; Ghaderi, E.; Shirazian, S. A.; Rahighi, R. Rolled graphene oxide foams as three-dimensional scaffolds for growth of neural fibers using electrical stimulation of stem cells. *Carbon* **2016**, *97*, 71−77.

(13) Sun, H.; Liu, Y.; Bai, X.; Zhou, X.; Zhou, H.; Liu, S.; Yan, B. Induction of oxidative stress and sensitization of cancer cells to paclitaxel by gold nanoparticles with different charge densities and hydrophobicities. *J. Mater. Chem. B* **2018**, *6* (11), 1633−1639.

(14) Li, R.; Guiney, L. M.; Chang, C. H.; Mansukhani, N. D.; Ji, Z.; Wang, X.; Liao, Y.-P.; Jiang, W.; Sun, B.; Hersam, M. C.; Nel, A. E.; Xia, T. Surface oxidation of graphene oxide determines membrane damage, lipid peroxidation, and cytotoxicity in macrophages in a pulmonary toxicity model. *ACS Nano* **2018**, *12* (2), 1390−1402.

(15) Lee, B.-M.; Seo, Y.-S.; Hur, J. Investigation of adsorptive fractionation of humic acid on graphene oxide using fluorescence EEM-PARAFAC. *Water Res.* **2015**, *73*, 242−251.

(16) Bhatnagar, A.; Sillanpää, M. Removal of natural organic matter (NOM) and its constituents from water by adsorption − A review. *Chemosphere* **2017**, *166*, 497−510.

(17) Jiang, Y.; Raliya, R.; Liao, P.; Biswas, P.; Fortner, J. D. Graphene oxides in water: assessing stability as a function of material and natural organic matter properties. *Environ. Sci.: Nano* **2017**, *4* (7), 1484−1493.

(18) Gao, S.; Zheng, X.; Hu, B.; Sun, M.; Wu, J.; Jiao, B.; Wang, L. Enzyme-linked, aptamer-based, competitive biolayer interferometry biosensor for palytoxin. *Biosens. Bioelectron.* **2017**, *89*, 952−958.

DOI: 10.1021/acs.est.8b05232
Environ. Sci. Technol. 2019, 53, 3773−3781

(19) Kumaraswamy, S., Tobias, R. Label-free kinetic analysis of an antibdy−antigen interaction using biolayer interferometry. In *Protein-Protein Interactions*; Humana Press: New York, 2015; pp 165−182.
(20) Chong, Y.; Ge, C.; Yang, Z.; Garate, J. A.; Gu, Z.; Weber, J. K.; Liu, J.; Zhou, R. Reduced cytotoxicity of graphene nanosheets mediated by blood-protein coating. *ACS Nano* **2015**, *9* (6), 5713−5724.
(21) Fang, G.; Luan, B.; Ge, C.; Chong, Y.; Dong, X.; Guo, J.; Tang, C.; Zhou, R. Understanding the graphene quantum dots-ubiquitin interaction by identifying the interaction sites. *Carbon* **2017**, *121*, 285−291.
(22) van den Kieboom, C. H.; van der Beek, S. L.; Mészáros, T.; Gyurcsányi, R. E.; Ferwerda, G.; de Jonge, M. I. Aptasensors for viral diagnostics. *TrAC, Trends Anal. Chem.* **2015**, *74*, 58−67.
(23) Apul, O. G.; Wang, Q.; Zhou, Y.; Karanfil, T. Adsorption of aromatic organic contaminants by graphene nanosheets: Comparison with carbon nanotubes and activated carbon. *Water Res.* **2013**, *47* (4), 1648−1654.
(24) Yang, K.; Xing, B. Adsorption of organic compounds by carbon nanomaterials in aqueous phase: Polanyi theory and its application. *Chem. Rev.* **2010**, *110* (10), 5989−6008.
(25) Chowdhury, I.; Duch, M. C.; Mansukhani, N. D.; Hersam, M. C.; Bouchard, D. Interactions of graphene oxide nanomaterials with natural organic matter and metal oxide surfaces. *Environ. Sci. Technol.* **2014**, *48* (16), 9382−9390.
(26) Aftab, B.; Hur, J. Fast tracking the molecular weight changes of humic substances in coagulation/flocculation processes via fluorescence EEM-PARAFAC. *Chemosphere* **2017**, *178*, 317−324.
(27) Omar, F. M.; Aziz, H. A.; Stoll, S. Aggregation and disaggregation of ZnO nanoparticles: Influence of pH and adsorption of suwannee river humic acid. *Sci. Total Environ.* **2014**, *15* (468−469), 195−201.
(28) McAdams, B. C.; Aiken, G. R.; McKnight, D. M.; Arnold, W. A.; Chin, Y.-P. High pressure size exclusion chromatography (HPSEC) determination of dissolved organic matter molecular weight revisited: accounting for changes in stationary phases, analytical standards, and isolation methods. *Environ. Sci. Technol.* **2018**, *52* (2), 722−730.
(29) Pansare, V. J.; Tien, D.; Thoniyot, P.; Prud'homme, R. K. Ultrafiltration of nanoparticle colloids. *J. Membr. Sci.* **2017**, *538*, 41−49.
(30) Ouyang, S.; Hu, X.; Zhou, Q.; Li, X.; Miao, X.; Zhou, R. Nanocolloids in natural water: isolation, characterization, and toxicity. *Environ. Sci. Technol.* **2018**, *52* (8), 4850−4860.
(31) Li, L.; Zhao, Z.; Huang, W.; Peng, P. a.; Sheng, G.; Fu, J. Characterization of humic acids fractionated by ultrafiltration. *Org. Geochem.* **2004**, *35* (9), 1025−1037.
(32) Hernandez, L. M.; Yousefi, N.; Tufenkji, N. Are there nanoplastics in your personal care products? *Environ. Sci. Technol. Lett.* **2017**, *4* (7), 280−285.
(33) Delley, B. From molecules to solids with the DMol3 approach. *J. Chem. Phys.* **2000**, *113* (18), 7756−7764.
(34) Lugo-Solis, A.; Vasiliev, I. Ab initio study of K adsorption on graphene and carbon nanotubes: Role of long-range ionic forces. *Phys. Rev. B: Condens. Matter Mater. Phys.* **2007**, *76* (23), 235431.
(35) Hammer, B.; Hansen, L. B.; Nørskov, J. K. Improved adsorption energetics within density-functional theory using revised Perdew-Burke-Ernzerhof functionals. *Phys. Rev. B: Condens. Matter Mater. Phys.* **1999**, *59* (11), 7413−7421.
(36) Delley, B. Hardness conserving semilocal pseudopotentials. *Phys. Rev. B: Condens. Matter Mater. Phys.* **2002**, *66* (15). DOI: 10.1103/PhysRevB.66.155125
(37) Sein, L. T.; Varnum, J. M.; Jansen, S. A. Conformational modeling of a new building block of humic acid: approaches to the lowest energy conformer. *Environ. Sci. Technol.* **1999**, *33* (4), 546−552.
(38) Mohr, S.; Ratcliff, L. E.; Genovese, L.; Caliste, D.; Boulanger, P.; Goedecker, S.; Deutsch, T. Accurate and efficient linear scaling DFT calculations with universal applicability. *Phys. Chem. Chem. Phys.* **2015**, *17* (47), 31360−31370.
(39) Duan, X.; Sun, H.; Ao, Z.; Zhou, L.; Wang, G.; Wang, S. Unveiling the active sites of graphene-catalyzed peroxymonosulfate activation. *Carbon* **2016**, *107*, 371−378.
(40) Duan, X.; Ao, Z.; Sun, H.; Indrawirawan, S.; Wang, Y.; Kang, J.; Liang, F.; Zhu, Z. H.; Wang, S. Nitrogen-doped graphene for generation and evolution of reactive radicals by metal-free catalysis. *ACS Appl. Mater. Interfaces* **2015**, *7* (7), 4169−4178.
(41) Li, X.; Mu, L.; Hu, X. Integrating proteomics, metabolomics and typical analysis to investigate the uptake and oxidative stress of graphene oxide and polycyclic aromatic hydrocarbons. *Environ. Sci.: Nano* **2018**, *5* (1), 115−129.
(42) Artz, R. R. E.; Chapman, S. J.; Campbell, C. D. Substrate utilisation profiles of microbial communities in peat are depth dependent and correlate with whole soil FTIR profiles. *Soil Biol. Biochem.* **2006**, *38* (9), 2958−2962.
(43) Zhao, X.; Wang, S.; Wang, Q.; Yao, H. Rheological and structural evolution of SBS modified asphalts under natural weathering. *Fuel* **2016**, *184*, 242−247.
(44) Zahra El Ouaqoudi, F.; El Fels, L.; Lemée, L.; Amblès, A.; Hafidi, M. Evaluation of lignocelullose compost stability and maturity using spectroscopic (FTIR) and thermal (TGA/TDA) analysis. *Ecol. Eng.* **2015**, *75*, 217−222.
(45) Bayer, C.; Martin-Neto, L.; Mielniczuk, J.; Saab, S. d. C.; Milori, D. M. P.; Bagnato, V. S. Tillage and cropping system effects on soil humic acid characteristics as determined by electron spin resonance and fluorescence spectroscopies. *Geoderma* **2002**, *105* (1), 81−92.
(46) Cai, N.; Peak, D.; Larese-Casanova, P. Factors influencing natural organic matter sorption onto commercial graphene oxides. *Chem. Eng. J.* **2015**, *273*, 568−579.
(47) Ateia, M.; Apul, O. G.; Shimizu, Y.; Muflihah, A.; Yoshimura, C.; Karanfil, T. Elucidating adsorptive fractions of natural organic matter on carbon nanotubes. *Environ. Sci. Technol.* **2017**, *51* (12), 7101−7110.
(48) Hyung, H.; Kim, J.-H. Natural organic matter (NOM) adsorption to multi-walled carbon nanotubes: effect of NOM characteristics and water quality parameters. *Environ. Sci. Technol.* **2008**, *42* (12), 4416−4421.
(49) Gotovac, S.; Honda, H.; Hattori, Y.; Takahashi, K.; Kanoh, H.; Kaneko, K. Effect of nanoscale curvature of single-walled carbon nanotubes on adsorption of polycyclic aromatic hydrocarbons. *Nano Lett.* **2007**, *7* (3), 583−587.
(50) Barba-Spaeth, G.; Dejnirattisai, W.; Rouvinski, A.; Vaney, M.-C.; Medits, I.; Sharma, A.; Simon-Lorière, E.; Sakuntabhai, A.; Cao-Lormeau, V.-M.; Haouz, A.; England, P.; Stiasny, K.; Mongkolsapaya, J.; Heinz, F. X.; Screaton, G. R.; Rey, F. A. Structural basis of potent *Zika−dengue virus* antibody cross-neutralization. *Nature* **2016**, *536* (7614), 48−53.
(51) Chowdhury, I.; Duch, M. C.; Mansukhani, N. D.; Hersam, M. C.; Bouchard, D. Colloidal properties and stability of graphene oxide nanomaterials in the aquatic environment. *Environ. Sci. Technol.* **2013**, *47* (12), 6288−6296.
(52) Chen, Y.; Ren, C.; Ouyang, S.; Hu, X.; Zhou, Q. Mitigation in multiple effects of graphene oxide toxicity in *Zebrafish* embryogenesis driven by humic acid. *Environ. Sci. Technol.* **2015**, *49* (16), 10147−10154.
(53) Hu, X.; Mu, L.; Kang, J.; Lu, K.; Zhou, R.; Zhou, Q. Humic acid acts as a natural antidote of graphene by regulating nanomaterial translocation and metabolic fluxes in *vivo*. *Environ. Sci. Technol.* **2014**, *48* (12), 6919−6927.
(54) Sun, Y.; Yang, S.; Zhao, G.; Wang, Q.; Wang, X. Adsorption of polycyclic aromatic hydrocarbons on graphene oxides and reduced graphene oxides. *Chem. - Asian J.* **2013**, *8* (11), 2755−2761.
(55) Joshi, R. K.; Carbone, P.; Wang, F. C.; Kravets, V. G.; Su, Y.; Grigorieva, I. V.; Wu, H. A.; Geim, A. K.; Nair, R. R. Precise and ultrafast molecular sieving through graphene oxide membranes. *Science* **2014**, *343* (6172), 752−754.

DOI: 10.1021/acs.est.8b05232
Environ. Sci. Technol. 2019, 53, 3773−3781

(56) Hu, X.; Mu, L.; Lu, K.; Kang, J.; Zhou, Q. Green synthesis of low-toxicity graphene-fulvic acid with an open band gap enhances demethylation of methylmercury. *ACS Appl. Mater. Interfaces* **2014**, *6* (12), 9220−9227.
(57) Cao, X.; Aiken, G. R.; Butler, K. D.; Mao, J.; Schmidt-Rohr, K. Comparison of the chemical composition of dissolved organic matter in three lakes in minnesota. *Environ. Sci. Technol.* **2018**, *52* (4), 1747−1755.
(58) Sun, C. Q.; Li, S.; Li, C. M. Impact of bond order loss on surface and nanosolid mechanics. *J. Phys. Chem. B* **2005**, *109* (1), 415−423.
(59) Wang, S.; Sun, H.; Ang, H. M.; Tadé, M. O. Adsorptive remediation of environmental pollutants using novel graphene-based nanomaterials. *Chem. Eng. J.* **2013**, *226* (24), 336−347.
(60) Ersan, G.; Apul, O. G.; Perreault, F.; Karanfil, T. Adsorption of organic contaminants by graphene nanosheets: A review. *Water Res.* **2017**, *126*, 385−398.

DOI: 10.1021/acs.est.8b05232
Environ. Sci. Technol. 2019, 53, 3773−3781